Very intense polarized emission in self-assembled room temperature metallomesogens based on Zn(ii) coordination complexes: an experimental and computational study

Massimo La Deda, Giuseppe Di Maio, Angela Candreva, Benoît Heinrich, Adelina-Antonia Andelescu, Evelyn Popa, Emilie Voirin, Valentin Badea, Mario Amati, Otilia Costişor, et al.

Very intense polarized emission in self-assembled room temperature metallomesogens based on Zn(II) coordination complexes: an experimental and computational study†

Massimo La Deda,[a] Giuseppe Di Maio,[a] Angela Candreva,[a] Benoît Heinrich,[b] Adelina-Antonia Andelescu,[c] Evelyn Popa,[c] Emilie Voirin,[b] Valentin Badea,[d] Mario Amati,[e] Otilia Costişor,[c] Bertrand Donnio*[b] and Elisabeta I. Szerb*[c]

[a] Department of Chemistry and Chemical Technologies, University of Calabria, Rende 87036, CS, Italy

[b] Institut de Physique et Chimie des Matériaux de Strasbourg (IPCMS), UMR7504, CNRS-Université de Strasbourg, Strasbourg 67034, France. E-mail: bertrand.donnio@ipcms.unistra.fr

[c] ''Coriolan Drăgulescu'' Institute of Chemistry, Romanian Academy, 24 Mihai Viteazu Bvd, Timisoara 300223, Romania. E-mail: eszerb@acad-icht.tm.edu.ro

[d] Department of Applied Chemistry and Organic and Natural Compounds Engineering, Politehnica University Timisoara, Carol Telbisz 6, Timisoara RO-300001, Romania

[e] Dipartimento di Scienze, Universita` degli Studi della Basilicata, Campus di Macchia Romana, Potenza 85100, Italy

J. Mater. Chem. C. **2022**, *10*, 115-125. DOI: 10.1039/d1tc05059a

Received: 20th October 2021; Accepted 10th November 2021

Abstract

Three room-temperature metallomesogens based on Zn(II) cations pentacoordinated by different chelating N^N^N terpyridines and two monodentate gallate co-ligands were designed and synthesized. Depending on the terpyridine ligand's tip functionality, the complexes self-assemble into either a 3D hexagonal mesophase or into a columnar hexagonal mesophase. A systematic study between the structure (molecular architecture, arrangement of the molecules and columns, and chains in both types of mesophases) and photophysical properties (emission maxima and yields, lifetimes of the excited states in the mesophase), correlated with investigations of single molecules in solution, was conducted. Remarkably, one complex exhibited a record quantum yield of 95.0% in solution, while in the mesophase, despite quenching due to the radiative deactivation from the ILCT state, still retained a considerable emission yield of ϕ = 20.2%. The polarized emission of an oriented film, determined for the first time in

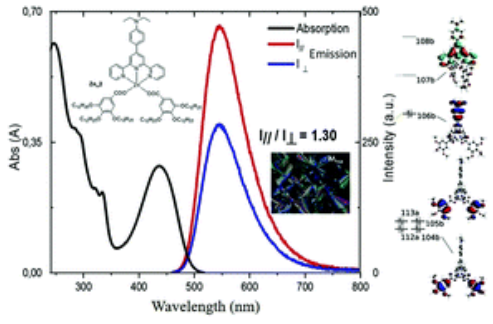

columnar metallomesogens, shows a dichroic emission ratio ($I_{||}/I_{\perp}$) of 1.30. DFT and TDDFT computational studies confirmed the origin of the observed fluorescence anisotropy from the transition dipole moment oriented along the C2 symmetry axis of the molecule combined with a high level of order in the 3D mesophase.

Introduction

Liquid crystals with intrinsic light-emitting properties are of great interest because such light-emitting materials may find a large variety of technological applications in various fields, such as OLEDs,[1] chemosensors,[2] optical information storage,[3] and liquid-crystal displays.[4] Despite these thrilling prospects, developing high-performance light-emitting liquid crystals remains a challenging task. Aggregation or self-organization is a spontaneous process in the formation of a mesophase, and incorporating luminophores into mesogens with preservation of both mesomorphism and luminescence properties is highly challenging.

Up to now, several synthetic strategies have been pursued with success to combine liquid crystal properties (*e.g.* anisotropy of the physical properties, fluidity, self-organization, dynamics, self-healing, and stimuli responsiveness) with high emission quantum yield materials. Of special interest here, the use of the unique optical properties of metal ions integrated in metallomesogens (MMs)[5] and lanthanidomesogens,[6] *i.e.* liquid crystalline *d*- and *f*-block metal coordination complexes, respectively, is one of such promising emerging approaches. Initially luminescence in the mesophase for MMs was somehow disregarded, mostly due to their high transition temperatures and poor thermal stabilities. In the last decade, the fine tuning of the molecular structure (nature of the metallic center, nature and functionalities of ligands, the presence of non-innocent counterions for ionic derivatives, *etc.*) to offer the right intermolecular interactions permitted a substantial decrease of the transition temperatures, obtaining low-temperature or even room-temperature MMs based on linearly coordinated Cu(I)[7] or Au(I)[7b,8] and Ag(I),[9] planar Au(III),[10] Pt(II) and Pd(II)[11] or Ni(II), Zn(II), and Cu(II)[12] and even for bulkier coordination geometries like tetrahedral or trigonal bipyramidal Zn(II),[13] Ag(I),[14] Cu(I),[15] octahedral Ir(III),[16] Ru(II)[17] or Rh(II)[18] metal centres.

Mesophase emission is due to either the intrinsic luminescence of the coordination compound, or is induced or enhanced in condensed states as a consequence of aggregation-induced emission (AIE).[19] The latter depends on the supramolecular arrangement or to the restriction of intramolecular motion (RIM),[20] due to high mesophase viscosity. In some cases, the luminescence of the coordination compounds is specifically due to a large pattern of conjugated aromatic rings of the ligands; therefore, the role of the metal is purely structural, as it confers stability to the compound, without modifying the electronic structure of the emissive state. Closed-shell *d*-metal ions, such as Zn(II), are ideal candidates to preserve the intense luminescence of polypyridinate molecules acting as ligands; therefore the challenge is to obtain liquid crystals of such complexes without turning the luminescence off.

Terpyridine (tpy) ligands are suitable for the construction of 2D and 3D programmable ordered “soft” and condensed supramolecular structures when coordinated to transition metals, yielding functional materials that gain interest in several application fields: stimuli responsive and/or self-healing supramolecular gels,[21] photoactive supramolecular architectures for optical devices,[22] MOFs, and catalysts.[23]

Previously we showed that lipophilic gallate could be a versatile unit for inducing liquid crystallinity in *d*-block metal coordination complexes[13b] eliminating several time consuming and money spending complex organic synthesis steps needed to functionalize ligands. Moreover, the presence of the electron donor benzoate group coordinated to a Zn(II) ion was found to considerably increase the emission quantum yield of the complex (24.5%) with respect to its dichloride precursor (6.4%) in solution. However, in condensed states, despite the reduction of non-radiative de-excitation pathways that occurred in the solid phase, a substantial reduction of the quantum yield (7.1%) due to different kinetics of the excited-state was observed. This prompted us to consider differently functionalized tpy ligands to fine-tune both the hexagonal arrangement in the mesophase and the excited state type, correlating changes in photophysical properties as a function of the supramolecular architecture.

Herein we report the synthesis and characterization of three new Zn(II) coordination complexes, **Zn_1-3** represented in Scheme 1, whose liquid crystallinity was induced through the use of two gallate monocoordinating units. The three complexes were mesomorphous over broad temperature ranges, showing a two-dimensional hexagonal columnar mesophase (Col_{hex}) or three-dimensional mesophase made of segmented columns (M_{hex}). Initially, we investigated the influence of the substituents on the liquid crystalline arrangements and on the luminescence, and then the molecular structure – supramolecular structure – photophysical property relationship. Finally, we selected the complex showing the highest emission quantum yield in the mesophase to evaluate the polarized emission. Polarized photoluminescence from a micropatterned film of columnar liquid crystals is rather difficult to observe, as it requires a high degree of orientational control, and furthermore the emission transition dipole moments give rise to a vector composition whose directions are much more difficult to correlate to the director than in classical nematic liquid crystals.[24] The obtained results show that the particular three-dimensional structure of **Zn_2** made it possible to obtain a remarkable emission anisotropy value.

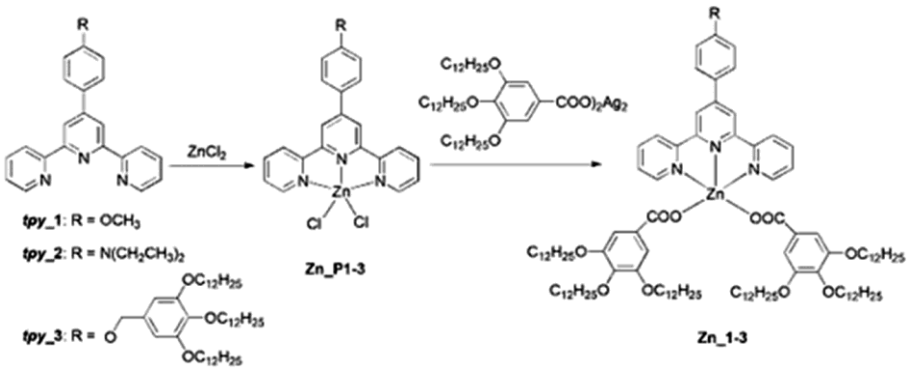

Scheme 1. Synthesis and chemical structure of Zn(II) precursor complexes **Zn_P1-3** and final complexes **Zn_1-3**.

Results and Discussion

Synthesis and structural characterization

Complexes **Zn_1-3** were synthesised following a route reported previously[13b] that required prior synthesis of Zn(II) dichloride precursors (**Zn_P1-3** in Scheme 1). All

Zn(II) complexes were obtained as white or yellow air stable solids in good yields (70–90%, see –the ESI†). The coordination of the carboxylate in an exclusive unidentate fashion was revealed by the separation of the stretching vibrations of the COO^- group (Δ) of 240–320 cm^{-1} (see Figures S3–S5, ESI†).[13b] The structures and purity of the final Zn(II) complexes were confirmed by elemental analysis, ^1H and ^{13}C NMR and MS (see the ESI†).

Mesomorphic properties

The thermal behavior was investigated by polarized optical microscopy (POM), differential scanning calorimetry (DSC) and thermal gravimetric analysis (TGA). The thermal properties are presented in Table 1 and in the ESI† (Figures S15–S20). Complexes **Zn_1-3** are room temperature liquid crystals with a wide range of mesophase existence.

By POM, complexes **Zn_1-3** show textures where hexagonal arrangement of columns can be envisaged from the occurrence of focal conic or mix mosaic textures (Figure 1) and to the presence of homeotropic zones. The complete authentication of the mesophases' type was nevertheless unambiguously achieved by S/WAXS (Small- and Wide-Angle X-ray Scattering) and Grazing Incidence Wide-Angle X-Ray Scattering (GIWAXS).

Table 1 Thermal data for Zn(II) complexes **Zn_1-3**

Cpd.	$T_{dec5\%}$[a] [°C]	Mesophases,[b] transition temperatures (°C) and enthalpies (ΔH [kJ·mol^{-1}])[c]
Zn_1	297	M_{hex} 229 [24.5] Iso / Iso 228 [28.0] M_{hex}
Zn_2	301	M_{hex} 188 [19.7] Iso / Iso 187 [25.1] M_{hex}
Zn_3	314	Col_{hex} 164 [19.7] Iso / Iso 167 [19.7] Col_{hex}

[a]Decomposition temperature at 5% weight-loss (from TGA); [b]M_{hex}: three-dimensional mesophase with a two-dimensional hexagonal lattice symmetry (see text), Col_{hex}: two-dimensional columnar hexagonal mesophase; [c]DSC data on second heating and cooling cycles.

In agreement with the POM observations and S/WAXS analysis (see below), **Zn_1** and **Zn_2** exhibit a three-dimensional mesophase (M_{hex}), and **Zn_3**, a two-dimensional hexagonal columnar mesophase (Col_{hex}). The M_{hex}/Col_{hex} transitions to isotropic liquid phase (Iso) are associated with significant enthalpy change and temperature delay, due to molecular self-assembly into cohesive mesomorphic structures. All complexes show transitions below room temperature to undefined mesomorphic and/or crystalline states (see Figures S18–S20, ESI†).

S/WAXS patterns are typical of liquid-crystalline phases, with scattering signals arising from liquid-like lateral distances between molecular segments in the wide-angle region (undifferentiated h_{ch} and h_{ar} signals for aliphatic and aromatic parts, respectively, and stacking periodicity of the molecules along the columns, h_{π}) and sharp small-angle reflections from the nanosegregated structure formed by the antagonistic aromatic and aliphatic segments (Figure 2 and Figures S21–S23, ESI†).

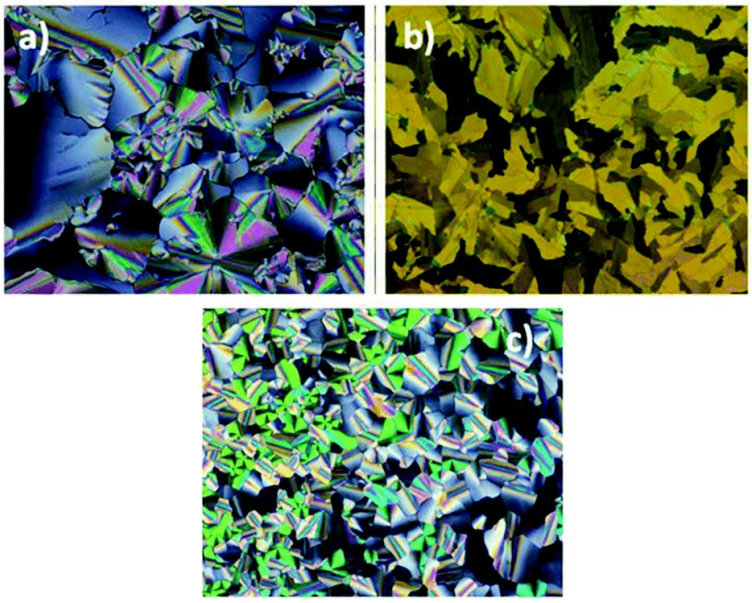

Figure 1. POM micrographs of the textures developed by complex (a) **Zn_1** on first cooling, 120 °C, magnification 20x; (b) **Zn_2** on first cooling, 50 °C, magnification 10x; (c) **Zn_3** on second cooling, 45 °C, magnification 20x.

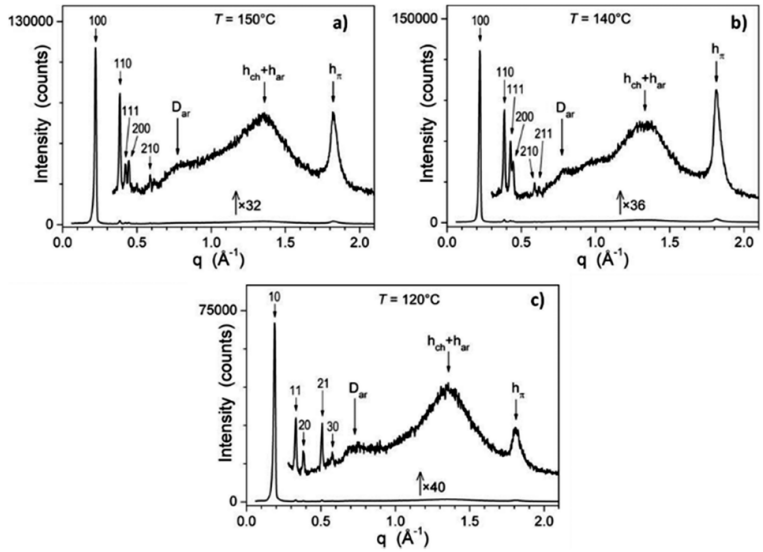

Figure 2. Indexed S/WAXS patterns of the Zn(II) complexes in the mesophases (*T*, temperature of the measurement): (a) **Zn_1** (M_{hex}); (b) **Zn_2** (M_{hex}); (c) **Zn_3** (Col_{hex}). Miller indices (*hk*) and (*hkl*) of the reflections, h_{ch}, h_{ar} and h_{π} signals arising from aliphatic, aromatic parts, and stacking periodicity, respectively (see the text).

Complex **Zn_3** self-assembles into columns surrounded by chains and forms a Col_{hex} structure, as evidenced by the semi-broad wide-angle signal h_{π} and the sharp small-angle reflections series (*hk*) of the hexagonal 2D-lattice. For the M_{hex} phase of **Zn_1** and **Zn_2**, (*hk*) series become (*hk*0) and coexist with crossed reflections (*hk*1) of a hexagonal 3D-structure resulting from the periodic segmentation of the columns. The geometrical parameters of the mesophases (lattice parameters *a* and *c*, cross-sectional areas, …) are gathered in Table 2, and do not vary much with temperature (see Table 2).

Table 2 Geometrical mesophase parameters[a]

Cpds Phase	*T*	V_{mol} ρ	*a* *A*[*Z*]	h_{mol} h_π	χχh A_{core}	M_{hex}	
						c *V*	Z_{mol}
						Col_{hex}	
						$D_{core,cyl}$ $S_{ZnAr,cyl}$	$s_{ch,cyl}$ $q_{ch,cyl}$
Zn_1 M_{hex}	20	2758 1.06	31.44 856[1]	3.22 3.36	0.714 245	36.40 31160	11.3
	50	2817 1.03	31.66 868[1]	3.24 3.37	0.715 248	36.50 31640	11.2
	150	3012 0.97	32.42 910[1]	3.31 3.45	0.717 257	35.49 32340	10.7
Zn_2 M_{hex}	20	2838 1.05	31.72 871[1]	3.26 3.39	0.722 242	33.70 29360	10.4
	60	2918 1.02	31.95 884[1]	3.30 3.41	0.723 244	34.35 30290	10.4
	140	3080 0.97	32.56 918[1]	3.35 3.46	0.725 252	34.08 31290	10.2
Zn_3 Col_{hex}	20	3862 1.02	37.23 1200[1]	3.22 3.38	0.754 295	19.4 196	21.8 1.02
	60	3973 1.00	37.58 1223[1]	3.25 3.42	0.755 297	19.5 199	22.1 1.01
	120	4141 0.96	37.75 1234[1]	3.36 3.47	0.756 301	19.6 206	22.9 1.00

[a] *T*, temperature of the measurement (°C); V_{mol}, molecular volume (Å^3); ρ, density (g/cm^3); *a*, lattice parameter; $A = a^2\sqrt{3}/2$, lattice area (Å^2); *Z*, number of columns per lattice; $h_{mol} = V_{mol}/A/Z$, molecular slice thickness (Å); h_π, π-stacking distance from peak position (Å); χ_{ch}, calculated aliphatic volume fraction; $A_{core} = (1-\chi_{ch})\times(A/Z)$, cross-sectional area of columnar cores (Å^2). For **Zn_1** and **Zn_2**: *c*, cell parameter (Å); $V = A\times c$, cell volume (Å^3); $Z_{mol} = V/V_{mol}$, number of molecules per cell. For **Zn_3**: $D_{core,cyl} = \sqrt{(4\times A_{core}/\pi)}$, core diameter (Å) of equivalent cylinder of cross-sectional area A_{core}; $S_{ZnAr,cyl} = \pi D_{core,cyl}\times h_{mol}$, cylinder surface area per Zn(II) complex (Å^2); $s_{ch,cyl} = S_{ZnAr,cyl}/n_{ch}$, cross-section area per chain (Å^2), n_{ch} being the number of peripheral substituents per molecule ($n_{ch} = 9$ for Zn_3); $q_{ch,cyl} = s_{ch,cyl}/\sigma_{ch}$, chain packing ratio for the average cylindrical interface.

The GIWAXS pattern of **Zn_2** thin film recorded at 20 °C (Figure 3) complies with a three-dimensional mesophase made of segmented columns of π-stacked complexes, ***a*** × ***b*** being the columnar plane and ***c*** the direction of stacking. Domains are oriented with the direction of columns parallel to the substrate and random in-plane orientation. Reflections were indexed in a three-dimensional hexagonal lattice. The space group of highest symmetry compatible with the presence of (*hk*1)/(*hh*1) reflections and absence of (*h*01)/(0*k*1) is $P6_3/mcm$. The space groups of lower symmetry with the same reflection conditions are *P*63*cm* and *P*6*c*2.

The geometry of the complexes can be deduced from single-crystal structures of molecules including the same complex moiety. Thus, structures of several Zn(ii) bis-(benzoato)-phenylterpyridine derivatives are available[25] and show irregular trigonal bipyramidal geometries, in which both benzoate ligands lie nearly orthogonal to the tpy ring plane.

In **Zn_1** and **Zn_2**, the pattern composition and geometrical parameters indicate that both compounds self-organize through π-stacking of tpy rings into columnar structures (Figure 4, left). The crowding of the long chains connected only on one side of the cores forces the complexes to stack on top of each other with rotation angles in the order of 120° that equally distribute chains and *R*-benzyloxyphenyl groups around the columnar cores. Consequently, the protruding benzyloxyphenyl moieties confer the

shape of a cross with three branches to the cross-section of columns. The columns, disposed at the nodes of the hexagonal lattice, adopt the most compact in-plane arrangement for this shape that consists in directing “crossed branches” toward “cross centers” of neighboring columns. This arrangement by nature follows the hexagonal symmetry but combines the segmentation of columns into smaller subunits. Only three over six neighboring columns are indeed pointed by crossed branches (due to the chains’ deficit on one side of the complex) and optimal space-filling presumably requires that pointed and non-pointed columns regularly swap along columnar axes, resulting in segmentation in groups of stacked molecules with inverted orientations. This segmentation defines the *P*6$_3$/*mcm* symmetry of the structure and the periodicity of two groups along the *c*-axis. It is found that the elementary group involves 5.6 **Zn_1** molecules and 5.2 **Zn_2** molecules.

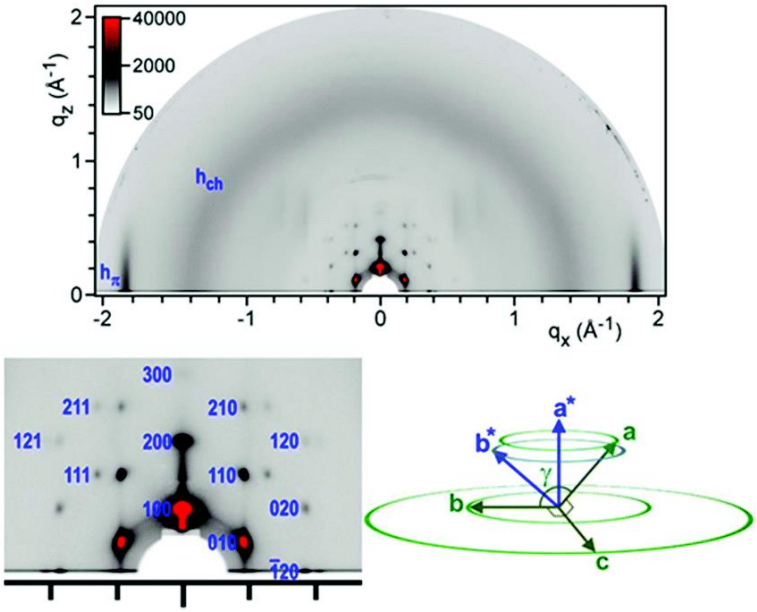

Figure 3. Top GIWAXS pattern of the **Zn_2** thin film at 20 °C that displays the scattering ring of the molten chain h_{ch}, a π-stacking spot h_π centered on the equator and reflection spots of a large-lattice structure; bottom left: expanded small-range region with indexation of reflections (blue labels on the right of the spots) and bottom right: orientations of cell axes in reciprocal space (blue) and direct space (green).

In **Zn_3**, beside the aliphatic chains introduced by the gallate units, three additional peripheral alkyl chains are introduced through the benzyloxyphenyl of the tpy ligand. This implies an expansion of the interface between antagonistic aromatic and alkyl chains segments and the aggregation of aromatic segments into columns surrounded by an aliphatic shell. The characteristic π-stacking signature h_π and the matching of the stacking distance with the molecular slice thickness h_{mol} further reveal that columnar cores consist of a single molecular strand of randomly orientated π-stacked tpy rings, each strand being located at the nodes of the hexagonal lattice. This strand is decorated with the gallate segments and *R*-benzyloxyphenyl groups of the individual complexes, whose average distances explain the additional broad scattering signals D_{ar} and h_{ar}. This decoration preserves the hexagonal lattice symmetry and the average interface with the aliphatic periphery is therefore a cylinder. Chain packing

ratio $q_{ch,cyl}$[26] is close to unity, *i.e.* nearly ideal for an efficient nanosegregation, which improves the cohesion of the structure and obviously contributes to the extended Col_{hex} range.

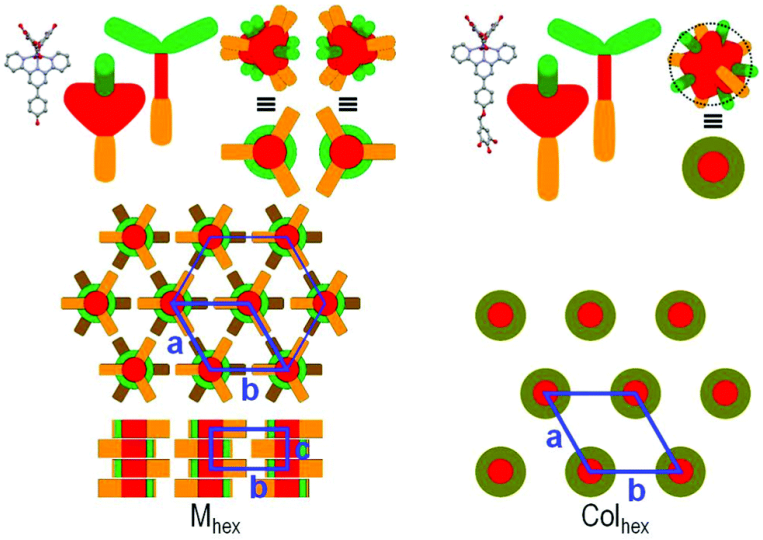

Figure 4. Left, top: view of the aromatic moiety of **Zn_1**, representations of the molecular architecture and of groups of π-stacked molecules; left, center: supramolecular self-assembly of **Zn_1** and **Zn_2** in the M_{hex} phase: hexagonal arrangement of groups of π-stacked molecules (chains not represented, dark green: groups from the layer below the top layer); left, bottom: superposition of groups of π-stacked molecules into a row of segmented columns. Right, top: view of the aromatic moiety of **Zn_3**, representations of the molecular architecture and of columns of π-stacked complexes surrounded by a shell mixing gallate and benzyloxyphenyl segments; right, bottom: arrangement of columns and chains (not represented) in the Col_{hex} phase.

Photophysics

The photophysical properties of **Zn_1-3** were collected from solutions and mesophase samples. The electronic states pattern is inferred from the spectra collected in diluted dichloromethane solutions (Figure 5 and Table 3). The absorption band below 280 nm is present in all the complexes and it is due to ligand-centred (LC) transitions on the gallate ligands[13*b*] (see for example in Figure S24 (ESI†) a comparison between the **Zn_2** and its dichloride precursor **Zn_P2** absorption spectra). The group of bands between 280 and 325 nm are attributed to charge-transfer (CT) transitions from the gallate to the tpy ligands (see the Computational results section).[13*b*,27] The band centered at 406 nm, present only in the **Zn_2** spectrum and responsible for the pale-green color of this sample, is due to a strong intraligand charge-transfer (ILCT) from the diethylaniline fragment to the aromatic rings of the tpy (see the Computational results section).[28]

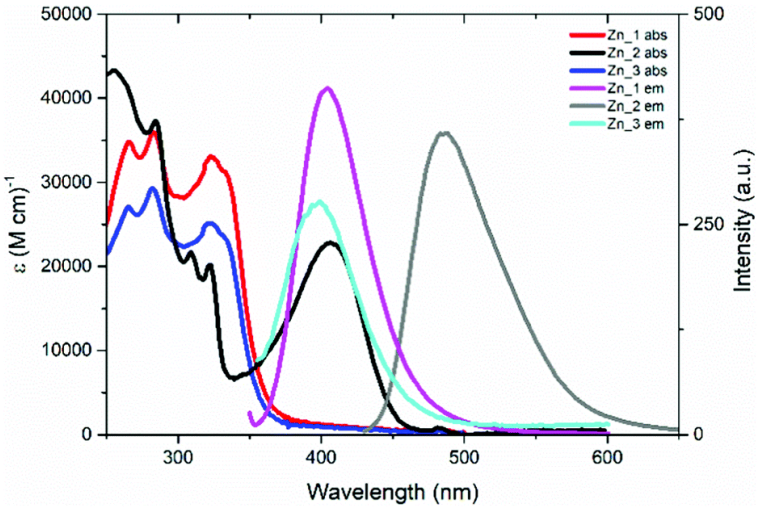

Figure 5. Absorption and emission spectra of **Zn_1-3** in diluted dichloromethane solution at room temperature ([**Zn_1**] = 4.3 × 10^{-6} M; [**Zn_2**] = [**Zn_3**] = 3.6 × 10^{-6} M). Excitation wavelength: 333 nm for **Zn_1** and **Zn_3**; 410 nm for **Zn_2**.

Table 3 Photophysical properties in CH_2Cl_2 solution

Sample	Abs, λ_{max}/nm (ε/M^{-1} cm^{-1})	Em, λ_{max}/nm	ϕ /%	τ /ns
Zn_1	266 (34820) 284 (35910) 323 (33160) 333 (31300)	405	6.5	2.0
Zn_2	255 (43320) 284 (37310) 309 (21770) 322 (20180) 406 (22830)	488	95.0	4.2
Zn_3	265 (27100), 282 (29320), 322 (25250), 333 (23410)	400	0.5	3.0

Fluorescence emission was registered for all samples. The emission from the CT excited state, observed for **Zn_1** and **Zn_3** at 405 and 400 nm, respectively, is weak, providing an emission quantum yield (ϕ) value of 6.5 and 0.5%, respectively. Interestingly, the fluorescence originated from the ILCT excited state in **Zn_2** (centered at 488 nm) reaches the outstanding ϕ-value of 95%. The decay from the excited state follows a first order kinetic for all samples, with lifetime values between 2.0 and 4.2 ns (see Table 3).

The effect of temperature variation on the photophysical properties of **Zn_1-3** in the mesophase is reported in Tables S1–S3 (ESI†). The reported data clearly show that after the first heating cycle, the values of the emission maximum and of the quantum yield have a little dependence on the temperature. In particular, the emission maximum wavelength remains fixed, throughout a wide temperature range (30–180 °C), while the emission quantum yield value, as expected, decreases with increasing temperature, due to the rise of non-radiative deactivation. This behaviour suggests that the temperature does not have a direct effect on the emission, but it depends on the supramolecular organization. For this reason, it is worth comparing the photophysical data of the mesophase and solutions at room temperature. Emission spectra recorded from mesophase samples at room temperature (Figure 6 and Table

4) have the same structure as those collected in solution. All suffer a red-shift with respect to the solutions, showing peaks at 435 nm for **Zn_1** (+30 nm) and **Zn_3** (+35 nm), and at 542 nm for **Zn_2** (+54 nm).

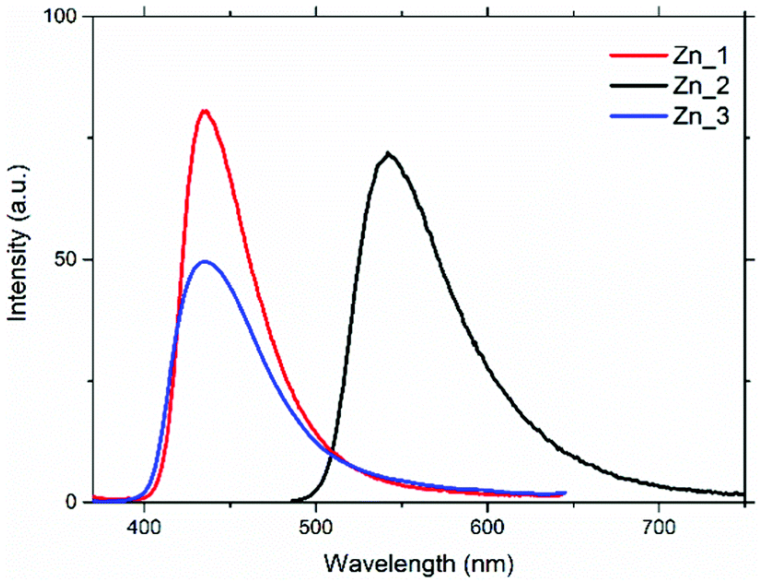

Figure 6. Emission spectra of the samples in the mesophase at room temperature. Excitation wavelength: 340 nm for **Zn_1** and **Zn_3**; 450 nm for **Zn_2**.

Table 4 Photophysical properties in the mesophase at room temperature

Sample	Em, λ_{max}/nm	ϕ /%
Zn_1	435	4.0
Zn_2	542	20.2
Zn_3	435	1.5

Compared to that measured in solution, the ϕ-value of **Zn_3** increases in the room-temperature mesophase (from 0.5 to 1.5%), while for **Zn_1** it decreases from 6.5 to 4.0%; for **Zn_2** it undergoes a drastic reduction from 95.0 to 20.2%. Generally, on going from solution to a condensed phase, the molecular packing reduces the vibrational motions and the consequent decrease of the non-radiative rate constant (k_{nr}) causes an increase in the luminescence intensity. While this statement is true for **Zn_3**, it is not for **Zn_1** and **Zn_2**.

Mesophase type of **Zn_3** (Col_{hex}) and of **Zn_1** and **Zn_2** (M_{hex}) exerts an effect on the quantum yield which adds to the reduction of vibrational motions. In fact, the columnar core of **Zn_1** and **Zn_2** consist of a three-molecule strand of π-stacked tpy rings, and this aggregation partially quenches luminescence; this is not effectively compensated by the reduction of k_{nr} and ultimately causes a reduction in the emission quantum yield for these compounds in the mesophase compared to the solution. In the columnar core of **Zn_3**, the poor π–π stacking does not effectively counterbalance the decrease in k_{nr}, and the quantum yield increases in the mesophase with respect to the solution. The

behaviour of **Zn_2** (which, as already highlighted, undergoes a drastic reduction of the ϕ-value) deserves a particular explanation, also considering that the mesophase is the same as **Zn_1**. This depends on the nature of the emissive state of this complex, which (unlike **Zn_1** and **Zn_3**) is an ILCT from the diethylaniline fragment to the aromatic rings of the tpy. This transition became partially symmetry-forbidden in the mesophase, where the packing distorts the orientation between the diethylaniline fragment and the tpy core, causing a noticeable reduction of the emission quantum yield.

Nevertheless, the luminescence quantum yield value of **Zn_2** remains considerable even in the mesophase, and for this reason the polarized emission of an oriented film of this complex was measured. To correlate the orientational order of the liquid crystal with its optical anisotropy properties, it is necessary to consider the orientation of the molecular emission transition dipole moment (TM) with respect to the columnar director. Theoretical calculations (see below) demonstrate that in the **Zn_2** molecule the TM vector lies on the plane of the aromatic rings of the tpy, oriented by the amino group towards the centre of gravity of the molecule.[29] Molecules form π-stacked units according to a symmetry that identifies a ternary axis parallel to the director, as shown in Figure 4, and the TMs point towards three directions placed at 120° from each other and perpendicular to the director. Considering that the π-stacked groups are offset by 60°, six TM vectors for each column (Figure 7a) can be identified. The M_{hex} phase hexagonal arrangement allows an ordered organization of the TMs, and therefore an emission anisotropy can be detected.

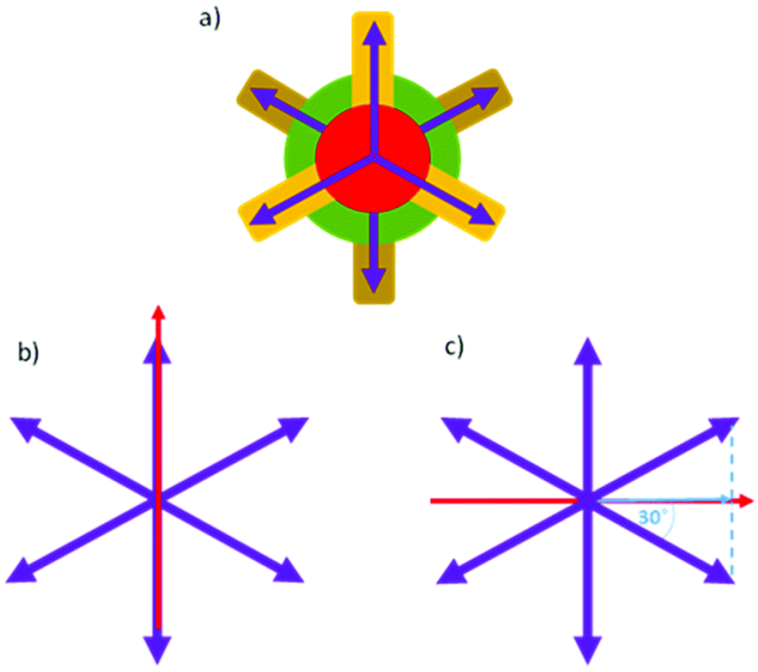

Figure 7. (a) Assumed orientation of the TMs (purple arrows) of **Zn_2** seen along the column axis (see Figure 4); (b) red arrow represents the direction of polarized emission light parallel to the TM; (c) red arrow represents the direction of polarized emission light perpendicular to the TM, while the blue arrow represents the projection of the vector TM along this direction.

Figure 8 reports the absorption and polarized emission spectra of the thin film of **Zn_2**, prepared as described in the ESI.†

The absorption spectrum of the film shows the same electronic transitions as those reported in Figure 5. Under un-polarised 440 nm excitation, the film shows a well-defined polarized emission band peaked at 546 nm, superimposable with that reported in Figure 6. When the emission polarizer (Figure 7b) is parallel (||) to the direction of one of the TM vectors (see the ESI†), the emission intensity is higher than when the polarizer (Figure 7c) is perpendicular (⊥), since in this last direction the TM vector projection is lower.

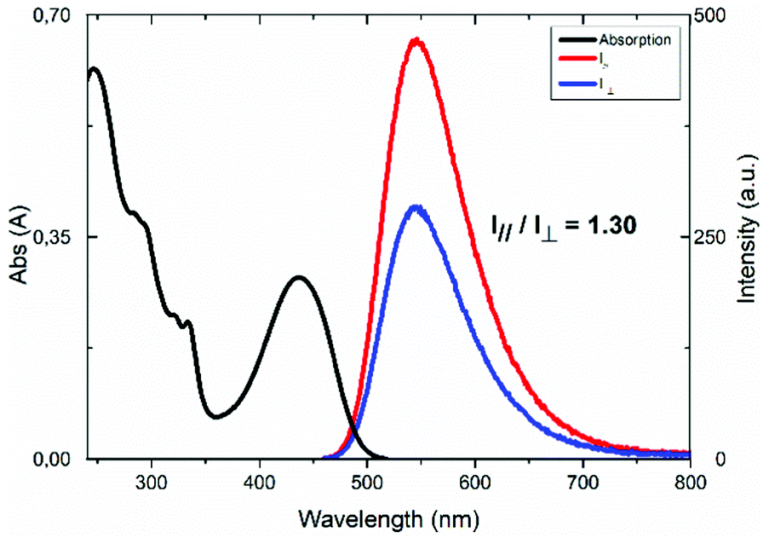

Figure 8. Absorption and polarized emission spectra of **Zn_2** on an aligned thin film at room temperature (||: parallel emission light; ⊥: perpendicular emission light; λ_{ex} = 440 nm).

The value of the $I_{||}/I_{\perp}$ ratio is 1.30, indicative of the average orientation of the luminescent liquid crystals, considering that the vector composition of the TMs always provide non-zero values of the emission intensity at each angular value; although this ratio is not high, this value is the first obtained for a columnar metallomesogen.

Computational results

Zn_1 and **Zn_2** were the object of computational investigations based on the DFT and TD-DFT methods (see “Computational methods” in the ESI†). In particular, the high fluorescence quantum yield of **Zn_2** and the fluorescence anisotropy in its mesophase were investigated.

In this respect, the main reference point for our theoretical study was the photophysical characterization performed in CH_2Cl_2 solutions. As evident in the following, inclusion of solvent effects is essential for the correct prediction of **Zn_2** spectroscopy. However, the particular nature of the studied complexes induces uncertainness about the way to model the environment. In fact, the presence of six long hydrocarbon chains surrounding the core of the complex can modify the solvation environment of the core itself. Our choice was to perform the computational studies on model systems in which

all the hydrocarbon chains were replaced with methyl groups and to carry out separate evaluations of the solvation effects by selecting *n*-hexane and CH_2Cl_2 as surrounding solvents. *n*-Hexane was used to simulate the hydrocarbon chains and the two solvents were chosen as extreme solvation environments, being the real environment in-between in terms of solute perturbation.

Figure 9 provides a visual description of the computed **Zn_2** structure. Its general features can be directly extended to **Zn_1** due to the great structural similarity between the two complexes. Table 5 lists some relevant structural parameters computed for **Zn_1** and **Zn_2** both in the gas phase and in CH_2Cl_2 solution. **Zn_2** belongs to the C_2 point symmetry. Accordingly, the three nitrogen aromatic donor atoms are labelled as C_2-axial (N_{ax}) and non-C_2-axial (N_{nax}). The coordination geometry can be considered trigonal bipyramidal (TBPY-5), with N_{ax} and both the O atoms of the gallate ligands in the equatorial plane of the bipyramid. An evident deviation from the ideal TBPY-5 coordination geometry is the N_{nax}–Zn–N_{nax} angle, which is significantly smaller than 180°. The computed structure is in line with the experimental structural analysis performed on similar complexes.[25] Analogue considerations can be applied to **Zn_1** (Table 5) which show a high level of local C_2 symmetry in most of its structure, in particular in the metal–ligands core of the complex. In both complexes, the phenyl group linked to the tpy core is rotated with respect to that of the tpy core itself. The dihedral angle between the average planes of the two aromatic systems (Ph and tpy in Table 5) are 36.2 and 38.6 degrees (**Zn_2** and **Zn_1** in vacuum, respectively) and it is reduced by 6–8 degrees in CH_2Cl_2.

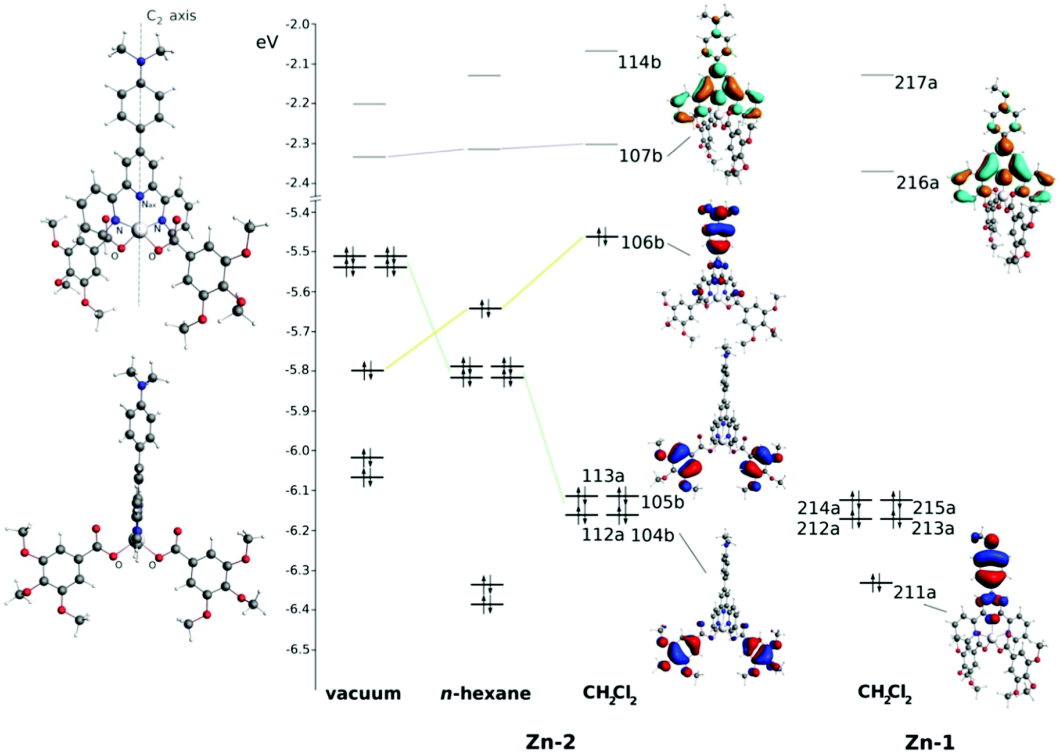

Figure 8. The computed structure of **Zn_2** (on the left) from two different viewpoints; energy levels (eV) of the **Zn_2** MOs computed in vacuum, *n*-hexane and CH_2Cl_2. The environmental-induced energy shift of the shown **Zn_2** MOs is evidenced by connecting lines. Some relevant orbitals are shown in correspondence of their energy level in CH_2Cl_2.

Table 5 Computed structural parameters (Å and degrees) of **Zn_1** and **Zn_2** in vacuum and in CH_2Cl_2 solution

	Zn_1		**Zn_2**	
	vacuum	CH_2Cl_2	vacuum	CH_2Cl_2
Zn-N_{ax}	2.133	2.104	2.127	2.097
Zn-N	2.238 2.239	2.224 2.225	2.240	2.226
Zn-O	1.969 1.970	1.992 1.992	1.971	1.991
N-Zn-N	148.3	149.8	148.4	150.0
O-Zn-O	105.6	98.8	105.4	98.1
O-Zn-N_{ax}	126.4 128.0	131.1 130.2	127.3	130.9
Ph-*tpy* dihedral angle	38.6	32.6	36.2	28.1

No relevant changes are attributed to solvation effects in comparison to computations in vacuum: the Zn–O bond distance increases by about 0.02 Å in CH_2Cl_2 by virtue of the increased solvation-induced stabilization of the "negatively charged" gallate ligands. As a consequence, the Zn–N bonds shorten by a similar amount. As expected, computed structural features in *n*-hexane are in-between the gas-phase and CH_2Cl_2 ones (Table S4 (ESI†) collects all the computed Cartesian coordinates).

Figure 9 sketches the molecular orbitals (MOs) energies of **Zn_2** and **Zn_1** computed in different environments which are important for the description of the low energy part of the absorption spectrum and also for the emission properties. In CH_2Cl_2, the **Zn_2** HOMO (Highest Occupied Molecular Orbital, 106b in Figure 9) is computed at −5.46 eV and is mainly localized on the diethylaniline group (86.5%). Lower in energy, in the range from −6.11 to −6.16 eV, gallate-localized MOs are present in the form of almost-degenerate symmetric (*A* symmetry) and corresponding asymmetric (*B* symmetry) combinations of the highest π bonding orbitals of gallate (for instance, 113a and 105b at −6.11 and −6.12 eV, respectively, only the asymmetric combination is shown in Figure 9). The **Zn_2** LUMO (Lowest Unoccupied Molecular Orbital, 107b in Figure 9) shows a larger localization on the tpy core (85.9%) with only small contributions from the diethylaniline group (8.0%). The contribution of the central metal atomic orbitals on all these MOs is negligible, being always lower than 1.2%. Passing from CH_2Cl_2 to *n*-hexane, the shape of the shown MOs does not significantly change but their energies shift in different ways. The gallate-localized MOs are destabilised as a consequence of the negative charge on them and the lower ability of *n*-hexane to polarize itself in the proximity. On the contrary, the HOMO (106b) is stabilized, being the polarization of the solvent less destabilizing on this part of the molecule in *n*-hexane (see Figure S25, ESI,† for details about the COSMO surface around the complex). Computations in vacuum show that the lack of solvation effects further destabilizes the gallate-localized MOs, which become the highest in energy occupied orbitals.

Differently from the occupied MOs, the LUMO is less affected by environmental effects, being mainly localized on the inner part of the tpy ligand and less exposed to the solvent in comparison to the diethylaniline and gallate ligands.

In **Zn_1**, MOs close to the HOMO and LUMO are very similar to the **Zn_2** ones. MO 211a corresponds to MO 106b in **Zn_2** (Figure 9). However, in **Zn_1**, the 211a MO is not the HOMO, neither in CH_2Cl_2, being lower in energy in comparison to the gallate-localized MOs (already described in **Zn_2** and found very similar also in **Zn_1**). This fact can be referred back to the lower π-conjugation of the OMe group (in comparison to the NEt_2) with the phenyl ring and also to the high electronegativity of the oxygen atom and consequently to its electron withdrawing ability. The **Zn_1** LUMO strongly resembles the **Zn_2** one, both in shape and in energy, because it is barely affected by the phenyl group and localized "internally" to the complex.

TD-DFT computations confirm the nature of the first singlet excited state (S_1) of **Zn_2** and **Zn_1** as already reported in the discussion of photophysical data in CH_2Cl_2 solution. **Zn_2** S_1 corresponds to an ILCT transition from the diethylaniline fragment to the tpy aromatic rings. In **Zn_1**, S_1 is predicted as a CT transition from the gallate to the tpy ligands. Table 6 lists some relevant features of S_1 of **Zn_2** and **Zn_1**. In **Zn_2**, S_1 can be assigned to a substantially pure HOMO–LUMO monoelectronic excitation (99.3% of contribution in CH_2Cl_2, 99.1% in *n*-hexane). The intensity of the related vertical electronic transition from the ground state (oscillator strength in Table 6) is computed to be rather large and it decreases passing from CH_2Cl_2 to the less polarizable *n*-hexane (in vacuum it is further lowered to 0.26, not reported in Table 6). Finally, being S_1 an *A*-symmetry state like the ground state, the transition dipole moment is fully directed along the C_2 axis of the molecule. All the higher singlet states (from S_2 to S_6) are characterised by a very low oscillator strength, hence no significant absorptions are predicted till 3.50 eV (354 nm, in CH_2Cl_2) or 3.13 eV (396 nm, in *n*-hexane). Thus, the low energy part of the **Zn_2** absorption spectrum is dominated by a single intense absorption toward S_1. In the experimental absorption spectrum (Figure 5 and Table 3), **Zn_2** differs from **Zn_1** and **Zn_3** for the presence of a well-defined band at 406 nm, which now can be safely assigned to the HOMO–LUMO transition. Interestingly, this absorption is computed at 452 nm in CH_2Cl_2, in good agreement with the experiment. However, the agreement improves when *n*-hexane is used as the solvent (418 nm). This could be an indication of the importance of the long hydrocarbon chains in determining the S_1 energy with respect to the ground state. As reported in Table 6, S_2 consists of an almost pure monoelectronic excitation from 106b (HOMO) to 114a, whereas the four following transitions consist of charge transfers from the gallate-localized MOs (112a, 113a, 104b and 105b) to the tpy-localized LUMO. The involved excited states consist of almost-degenerate couples of *A* and *B* symmetry states (for instance S_3 and S_4). For symmetry reasons, the transition dipole moment of the B states is perpendicular to the C_2 rotation axis.

Table 6 Computed lowest-energy singlet excited states properties

State	Energy	Oscillator Strength	Composition
Zn_2 (n-hexane solution)			
S1 (2A)	2.74 eV; 452 nm	0.59	106b -> 107b 99.3%

S2 (1B)	2.90 eV; 428 nm	2.6·10-4	106b -> 114a 99.1%
S3 (2B)	3.44 eV; 360 nm	4.5·10-5	113a -> 107b 99.8%
S4 (3A)	3.44 eV; 360 nm	9.6·105	105b -> 107b 99.8%
S5 (3B)	3.50 eV; 354 nm	3.7·10-5	112a -> 107b 99.8%
S6(4A)	3.50 eV; 350 nm	3.6·10-4	104b -> 107b 99.8%
Zn_1 (CH_2Cl_2 solution)			
S1	3.38 eV; 367 nm	3.1·10-5	215a -> 216a 68.8% 214a -> 216a 31.1%
S2	3.38 eV; 367 nm	1.2·10-4	215a -> 216a 31.1% 214a -> 216a 68.8%
S3	3.44 eV; 360 nm	1.3·10-4	213a -> 216a 94.3%
S4	3.44 eV; 360 nm	9.1·10-6	212a -> 216a 94.3%
S5	3.47 eV; 357 nm	0.56	211a -> 216a 98.7%
S6	3.63 eV; 342 nm	8.6·10-5	215a -> 217a 66.5% 214a -> 217a 31.4%

Passing to **Zn_1**, low-intensity gallate-to-tpy CTs become the lowest electronic transitions (Table 6). The intense tpy-centred absorption is now associated to S_5 rather than S_1, and it is predicted at 357 nm, in good agreement with the first intense features measured at 333 nm (Table 3). Interestingly, the weak absorption around 400 nm (appearing like a tail at lower energies respect to the first absorption band in Figure 5) confirms the presence of lower in energy singlet states (from S_1 to S_4) with low absorption intensities. This tail is not visible in the **Zn_2** spectrum, a fact that further confirms the accuracy of the performed computations.

At this point we are able to explain the differences in fluorescence properties between **Zn_2** and **Zn_1**. The first difference is the fluorescence quantum yield. **Zn_2** is strongly emissive due to the large oscillator strength (transition dipole moment) of S_1 in this complex, which leads to fast fluorescence kinetics. In **Zn_1**, on the contrary, the lowest singlet states are different and associated to very low oscillator strengths. Accordingly, they are barely emissive due to unfavourable electronic properties. Also, the longer emission wavelength in **Zn_2** can be easily explained as a consequence of the lower HOMO–LUMO gap in comparison to **Zn_1**. In this case, a key role is played by the NEt_2 substituent of the diethylaniline of **Zn_2**, which is able to destabilize the phenyl-localized π MOs much more than the OMe group in **Zn_1**.

Zn_3 is expected to be similar to **Zn_1** in terms of electronic structure and (consequently) spectroscopy. The coupling between the OR substituent and the phenyl group in the tpy-based fragment is likely to be comparable to the OMe coupling in **Zn_1**. This prediction is corroborated by the similarity in absorption and emission spectroscopy between **Zn_3** and **Zn_1** (see Figure 5).

Now it is possible to explain the observed fluorescence anisotropy from the **Zn_2** mesophase. In the previous paragraph, this observation was supposed to be originated by a transition dipole moment oriented along the metal-tpy direction,

obviously combined to a high level of order in the columnar arrangement of the liquid crystal. This is in perfect agreement with the computational results. As discussed previously, in **Zn_2** the emission transition dipole must be directed along the C_2 symmetry axis of the molecule (Figure 9), like the absorption transition dipole associated to S_1. This is imposed by symmetry, since the first excited state is of *A* symmetry.

Conclusions

With the increased importance in obtaining functional optical materials for practical applications, luminescent metallomesogens are promising for the next generation of emitters. The research is highly challenging due to the necessity of matching the structural requirements for inducing mesomorphic properties, high luminescence properties and fine tuning of mesophase architecture for preserving or improving the molecular properties. Among liquid crystal architectures, a columnar one is pivotal for electrical conduction; however, it may be detrimental for the metallomesogen optical properties, favouring quenching of luminescence due to the formation of new excited states by the close packing of emitters. On the other hand, its high viscosity that increases its rheological stability, favour aggregation induced emission as a result of RIM.

Therefore we designed and synthesized new room temperature metallomesogens based on bio-available low-cost Zn(ii) ions through the monodentate coordination of two lipophilic gallate units. The complexes show different 3D (**Zn_1** and **Zn_2**: M_{hex}) or 2D (**Zn_3**: Col_{hex}) liquid crystalline columnar organizations as a function of the functional group inserted on the chelating *N^N^N* terpyridine ligand.

Systematic structural, computational and photophysical studies allowed the correlation between liquid crystalline architecture and emitting properties in the mesophase. While complexes **Zn_1** and **Zn_3** emit modestly, the fluorescence originated from the ILCT excited state in **Zn_2** from the electron-donating $–NEt_2$ group to the electron-withdrawing aromatic rings of the tpy ligand reach a record luminescence quantum yield in solution (95%). Although the efficiency is reduced in the mesophase due to distortion of the diethylaniline with respect to the aromatic rings of tpy, it still remains as high as 20%.

Taking advantage of this high emission quantum yield of the mesophase, the polarized fluorescence of an oriented film of a columnar metallomesogen was measured for the first time, giving a $I_{\parallel}/I_{\perp}$ ratio of 1.30, while theoretical calculations on the orientation of the transition dipole moment support the discussion.

Authors contribution

Conceptualization, M. L. D., B. D., M. A. and E. I. S.; methodology, E. I. S.; investigation, G. D. M., A. C., B. H., A. A. A., E. P., E. V., V. B. and M. A.; resources, E. I. S.; data curation, M. L. D., B. H., M. A., B. D. and E. I. S.; writing – original draft M. L. D., M. A., O. C., B. D. and E. I. S.; writing – review and editing, M. L. D., M. A., B. D. and E. I. S.

Supplementary data

† Electronic supplementary information (ESI) available: Experimental section, synthesis and characterization, FT-IR spectra of complexes **Zn_1-3**, ^{1}H and ^{13}C NMR spectra of complexes **Zn_1-3**, mass spectra of complexes **Zn_1-3**, TGA traces of precursor complexes **Zn_P1-3** and complexes **Zn_1-3**, DSC traces of complexes **Zn_1-3**, S/WAXS patterns of complexes **Zn_1-3**, photophysical data of complexes **Zn_1-3**, and computational studies. See DOI: 10.1039/d1tc05059a

Acknowledgements

This work was supported by a grant of the Romanian Ministry of Education and Research, CNCS – UEFISCDI, project number PN-III-P4-ID-PCE-2020-1958, within PNCDI III. Italian Ministry of University and Research supported this research through DEMETRA project (PON ARS01_00401). We thank Pohang Accelerator Laboratory (PAL) for giving us the opportunity to perform the GIWAXS experiment, MEST and POSTECH for supporting this experiment, Dr Hyungju Ahn for adjustment of beamline and for doing the measurement. A. A. A., E. P., E. I. Sz. and O. C. acknowledge the Romanian Academy, Program 4. A. A. A. is grateful for the "Ion Heliade Radulescu" mobility scholarship. We acknowledge the Laboratoire de Spectrométrie de Masse BioOrganique (LSMBO) IPHC UMR 7178 for mass spectrometry analysis. BD and BH thank CNRS and the University of Strasbourg for support.

References

1 a) C. Keum, D. Becker, E. Archer, H. Bock, H. Kitzerow, M. C. Gather and C. Murawski, *Adv. Optical Mater*., 2020, 2000414; b) G. Qian, X. Yang, X. Wang, J. D. Herod, D. W. Bruce, S. Wang, W. Zhu, P. Duan and Y. Wang, *Adv. Optical Mater*., 2020, **8**(20), 2000775; c) J. De, W.-Y. Yang, I. Bala, S. P. Gupta, R. A. K. Yadav, D. K. Dubey, A. Chowdhury, J.-H. Jou and S. K. Pal, *ACS Appl. Mater. Interfaces,* 2019, **11**, 8291; d) J. Han, S. Guo, H. Lu, S. Liu, Q. Zhao, W. Huang, *Adv. Optical Mater.,* 2018, 1800538; e) Y. Wang, J. Shi, J. Chen, W. Zhu and E. Baranoff, *J. Mater. Chem. C,* 2015, **3**, 7993; f) Y. Wang, J. Fan, J. Shi, H. Qi, E. Baranoff, G. Xie, Q. Li, H. Tan, Y. Liu, W. Zhu *Dyes Pigm*., 2016, **133**, 238.

2 a) X. Hao, B. Xiong, M. Ni, B. Tang, Y. Ma, H. Peng, X. Zhou, I. I. Smalyukh and X. Xie, *ACS Appl. Mater. Interfaces,* 2020, **12**, 53058; b) C. Cuerva, J. A. Campo, P. Ovejero, M. R. Torres, E. Oliveira, S. M. Santos, C. Lodeiro and M. Cano, *J. Mater. Chem. C.,* 2014, **2**(43), 9167.

3 Y. L. Zhuang, X. L. Ren, X. T. Che, S. J. Liu, W. Huang and Q. Zhao, *Advanced Photonics,* 2021, **3**(1), 014001.

4 a) H.-W. Chen, J.-H. Lee, B.-Y. Lin, S. Chen and S.-T. Wu, *Light: Science & Applications,* 2018, **7,** 17168; b) D. Zhao, H. He, X. Gu, L. Guo, K. S. Wong, J. W. Y. Lam and B. Z. Tang *Adv. Optical Mater.,* 2016, **4**, 534.

5 a) D. Pucci and B. Donnio in Handbook of Liquid Crystals: Metal-containing liquid crystals, Vol 5: Non-Conventional, Supramolecular, Chromonic and Amphiphilic Liquid Crystals. (Eds. J. W. Goodby, P. J. Collings, T. Kato, C. Tschierske, H. Gleeson, P. Raynes), Wiley-VCH Weinheim 2014, ISBN: 9783527671403; b) C. Cuerva, M. Cano and C. Lodeiro, *Chem. Rev*. 2021, **121**, 20, 12966.

6 K. Rajendiran, S. T. Yoganandham, S. Arumugam, D. Arumugam and K. Thananjeyan, *J. Molec. Liq.,* 2021, **321**, 114793.

7 a) R. Giménez, |O. Crespo, B. Diosdado and A. Elduque, *J. Mater. Chem. C* 2020, **8**, 6552; b) A. Kishimura, T. Yamashita, K. Yamaguchi and T. Aida, *Nat. Mater.,* 2005, **4**, 546; c) R. Chico, C. Dominguez, B. Donnio, B. Heinrich, S. Coco and P. Espinet, *Cryst. Growth Des.,* 2016, **16**(12), 6984-6991.

8 E. Beltrán, J. Barberá, J. L. Serrano, A. Elduque and R. Giménez Phase, *Eur. J. Inorg. Chem.,* 2014, 1165–1173.

9 a) J. Jiménez, J. A. Sanz, J. L. Serrano, J. Barberá and L. Oriol *Inorg. Chem.,* 2020, **59**(7), 4842; b) P. Dechambenoit, S. Ferlay, B. Donnio, D. Guillon and M.W. Hosseini, *Chem. Commun.,* 2011, **47**, 734-736.

10 R. R. Parker, D. H. Liu, X. K. Yu, A. C. Whitwood, W. G. Zhu, J. A. G. Williams, Y. F. Wang, J. M. Lynam and D. W. Bruce, *J. Mater. Chem. C*, 2021, **9**(4), 1287.

11 a) G. Qian, X. Yang, X. Wang, J. D. Herod, D. W. Bruce, S. Wang, W. Zhu, P. Duan and Y. Wang, *Adv. Optical Mater*., 2020, 2000775; b) B. Yang, H. Ni, H. Wang, Y. Hu, K. Luo and W. Yu, *J. Phys.*

Chem. C., 2020, **124**(43), 23879; c) L. Zhao, B. Yang, L. Zeng, K. Luo, H. Wang, H. Ni, C. Yang and Q. Li, *Dyes Pigm.,* 2019, **164**, 398; d) C. Cuerva, J. A. Campo, M. Cano and C. Lodeiro, *Chem. Eur. J*., 2019, **25**(52), 12046; e) C. Cuerva, J. A. Campo, M. Cano, R. Schmidt and C. Lodeiro, *J. Mater. Chem. C*, 2018, **2**, 9723; f) E. Tritto, R. Chico, J. Ortega, C. L. Folcia, J. Etxebarria, S. Coco and P. Espinet, *J. Mater. Chem. C,* 2015, **3**(36), 9385; g) V. N. Kozhevnikov, B. Donnio, D. W. Bruce, *Angew. Chem., Int. Ed*., 2008, **47**, 6286.

12 a) E. de Domingo, C. L. Folcia, J. Ortega, J. Etxebarria, R. Termine, A. Golemme, S. Coco and P. Espinet, *Inorg. Chem*., 2020, **59**(15)*,* 10482; b) M. Park, D.-G. Kang, H. Ko, M. Rim, D. T. Tran, S. Park, M. Kang, T.-W. Kim, N. Kim and K.-U. Jeong, *Mater. Horizons,* 2020, **7**(10), 2635; c) S. Chakraborty, S. K. Prasad, D. S. S. Rao and C. R. Bhattacharjee, *Liq. Cryst.,* 2019, **46**(6), 872; d) R. Zhang, H. Gao, Y. Ren, Y. Xiao, J. Hu and X. Cheng, *Chem. Asian J.,* 2018, **13**(5), 536; e) S. Chakraborty, P. Mondal, S. K. Prasad, D. S. S. Rao and C. R. Bhattacharjee, *Eur. J. Inorg. Chem.,* 2016, 4604; f) S. Debnath, H. F. Srour, B. Donnio, M. Fourmigué and F. Camerel, *RSC Adv,*. 2012, **2**, 4453; g) C. Cretu, L. Cseh, B. J. Tang, V. Sasca, V. Badea, E. I. Szerb, G. Mehl, S. Shova and O. Costisor, *Liq. Cryst.,* 2015, **42**, 1139.

13 a) N. S. S. Kumar, M. Z. Shafikov, A. C. Whitwood, B. Donnio, P. B. Karadakov, V. N. Kozhevnikov and D. W. Bruce, *Chem. Eur. J.,* 2016, **22**, 8215; b) A.-A. Andelescu, B. Heinrich, M. A. Spirache, E. Voirin, M. La Deda, G. Di Maio, E. I. Szerb, B. Donnio and O. Costisor, *Chem. Eur. J.,* 2020, **26**, 4850; c) D. Pucci, A. Crispini, M. Ghedini, M. La Deda, P. F. Liguori, C. Pettinari and E. I. Szerb, *RSC Advances,* 2012, **2**, 9071.

14 a) L. Soria, P. Ovejero, M. Cano, J. A. Campo, M. R. Torres, C. Núñez and C. Lodeiro, *Dyes Pigm*., 2014, **110**, 159; b) D. Pucci, A. Crispini, M. Ghedini, E. I. Szerb and M. La Deda, *Dalton Trans.,* 2011, **40**, 4614.

15 C. Cretu, A. A. Andelescu, A. Candreva, A. Crispini, E. I. Szerb and M. La Deda, *J. Mater. Chem. C,* 2018, **6,** 10073.

16 a) G. Zou, L. Zhao, L. Zeng, K. Luo, H. Ni, H. Wang, Q. Li, W. Yu and X. Li, *Inorg. Chem.,* 2019, **58***, 1*, 861; b) A. M. Prokhorov, A. Santoro, J. A. G. Williams and D. W. Bruce, *Angew. Chem. Int. Ed.,* 2012, **51**, 95; c) E. I. Szerb, A. M. Talarico, I. Aiello, A. Crispini, N. Godbert, D. Pucci and T. Pugliese, *Eur. J. Inorg. Chem*., 2010, 3270.

17 a) H. Ishida, M. Handa, I. Hiromitsu, S. Ujiie, D. Yoshioka, R. Mitsuhashi and M. Mikuriya, *New J. Chem.* 2019*,* **43**, 1134; b) D. Pucci, A. Bellusci, A. Crispini, M. Ghedini, N. Godbert, E. I. Szerb and A. M. Talarico, *J. Mater. Chem.* 2009, **19**, 7643.

18 L. Rossi, C. Huck-Iriart, M. A. Castro and F. D. Cukiernik, *J. Coord. Chem.,* 2017, **70**(21), 3633.

19 P. Alam, C. Climent, P. Alemany and I. R Laskar, *J. Photochem. Photobiol. C*, 2019, **41**, 100317.

20 T. Shu, J. Wang, L. Su and X. Zhang, *Crit. Rev. Anal. Chem.,* 2018, **48**(4), 330.

21 P. Peng, Y. Li, W. Song and X. Yu, *Colloids Surf. A Physicochem. Eng. Asp,* 2020**, 589**, 124439.

22 A. Agosti, E. Kuna and G. Bergamini, *Eur. J. Inorg. Chem.,* 2019, **2019**, 577.

23 a) A. Winter and U. S. Schubert, *ChemCatChem,* 2020, **12**, 2890; b) C. Wei, Y. He, X. Shi and Z. Song, *Coord. Chem. Rev.,* 2019, **385**, 1; c) Y. H. Budnikova, D. A. Vicic and A. Klein *Inorganics,* 2018**, 6**(1), 18.

24 a) S. Furumi, D. Janietz, M. Kidowaki, M. Nakagawa, S. Morino, J. Stumpe and K. Ichimura, *Chem. Mater.,* 2001, **13**, 1434; b) S. Zimmermann, J. H. Wendorff and C. Weder, *Chem. Mater.,* 2002, **14***,* 2218.

25 The Cambridge Structural Database. Z. Ma, W. Lu, B. Liang and A. J. L. Pombeiro, *New. J. Chem*., 2013, **37**, 1529.

26 D. Myśliwiec, B. Donnio, P. J. Chmielewski, B. Heinrich and M. Stępień, *J. Am. Chem. Soc,* 2012**, 134**, 4822.

27 a) X. Chen, Q. Zhou, Y. Cheng, Y. Geng, D. Ma, Z. Xie and L. Wang *J. Lumin*., 2007, **126**, 81; b) W. Goodall and J. A. G. Williams, *Chem. Commun.,* 2001, 2514.

28 X. Bi and Y. Pang, *J. Phys. Chem. B* 2016, **120**(13), 3311.

29 a) A. Winter, C. Friebe, M. Chiper, M. D. Hager and U. S. Schubert, *J. Polym. Sci. A: Polym. Chem.* 2009, **47**, 4083; b) I. Eryazici, C. N. Moorefield and G. R. Newkome, *Chem. Rev.* 2008, **108**, 1834; c) M. Humbert-Droz, C. Piguet and T. A. Wesolowski, *Phys. Chem. Chem. Phys.*, 2016, **18**, 29387.